

# “Look-Ahead Distance” of a fiber probe used to assist neurosurgery: *Phantom and Monte Carlo study*

Zhiyu Qian<sup>1,2</sup>, Sunder S. Victor<sup>1</sup>, Yueqing Gu<sup>1</sup>, Cole A. Giller,<sup>3</sup> Hanli Liu<sup>1</sup>

<sup>1</sup>*Biomedical Engineering, University of Texas at Arlington, Arlington, Texas, 76019*

<sup>2</sup>*Institute of Smart Material and Structure, Nanjing University of Aeronautics and Astronautics, Nanjing, China, 210016*

<sup>3</sup>*Department of Neurological Surgery, University of Texas Southwestern Medical Center at Dallas, Texas 75390*

[hanli@uta.edu](mailto:hanli@uta.edu)

**Abstract** A short-separation, optical reflectance probe has been developed to assist the neurosurgeon in functional neurosurgery for accurate localization of the surgical target. Because of the scattering nature of tissue, the optical probe has a “Look Ahead Distance” (LAD), at which the measured optical reflectance starts to “see” or “sense” the underlying brain structure due to the difference in light scattering of tissue. To quantify the LAD, 2-layer laboratory phantoms have been developed to mimic gray and white matter of the brain, and Monte Carlo simulations have been also used to confirm the experimental findings. Based on both the laboratory and simulation results, a quantitative empirical equation is developed to express the LAD as a function of scattering coefficient of the measured tissue for a 400-micron-diameter fiber probe. The quantified LAD of the probe is highly desirable so as to improve the spatial resolution of the probe for better surgery guidance.

©2003 Optical Society of America

**OCIS codes:** Fiber Optic Probe, Monte Carlo Simulations, Reduced Scattering Coefficient, Tissue phantoms, Neurosurgery, Light Scattering from Tissue

---

## References and Links

1. M. G. Nichols, E. L. Hull, and T. H. Foster, “ Design and testing of a white-light, steady-state diffuse reflectance spectrometer for determination of optical properties of highly scattering systems,” *Appl. Opt.* **36**, 93-103 (1997).
2. T. J. Farrell and M. S. Patterson “A diffusion theory model of spatially resolved, steady-state diffuse reflectance for the noninvasive determination of tissue optical properties in vivo,” *Med. Phys.* **19**, 880-888 (1992).
3. M. Johns, Cole A. Giller, and H. Liu, “Computational and in vivo Investigation of Optical Reflectance from Human Brain to Assist Neurosurgery,” *J. Biomed. Opt.* **3**, 437-445 (1998).
4. D. A. Benaron, W. Cheong, J. L. Duckworth, K. Noles, C. Nezhat, D. Seidman, S. R. Hintz, C. J. Levinson, A. L. Murphy, J. W. Price, F. W. H. Liu, D. K. Stevenson, E. L. Kermit, *OSA TOPS* **22**, 30-34 (1998).
5. R. Richards-Kortum, “Quantitative optical spectroscopy for tissue diagnosis,” *Annu. Rev. Phys. Chem.* **47**, 555-606 (1996)
6. J. R. Mourant, I. J. Bigio, J. Boyer, R. L. Conn, T. Johnson and T. Shimada, *Lasers Surg. Med.*, **17**, 350-357 (1995).
7. J. R. Mourant, T. Johnson, G. Los, and I. J. Bigio, *Phys. Med. Biol.* **44**, 1397-1417 (1999).
8. L. Reynolds, C. Johnson, and A. Ishimaru, “Diffuse reflectance from a finite blood medium: applications to the modeling of fiber optical catheters,” *Appl. Opt.* **15**, 2059-2067 (1976).
9. J.M. Steinake and A.P. shepherd, “ Diffusion model of the optical absorbance of whole blood,” *J. Opt. Soc. Am. A* **7**, 813-822 (1998).

10. B. J. Tromberg, R. C. Haskell, S. J. Madson, and L. O. Svaasand, "Characterization of tissue optical properties using photon density waves," *Comments Mol. Cell. Biophys.* **8**, 359-385 (1995).
11. C.E. Elwell, M. Cope, A.D. Edwards, J. S. Wyatt, D. T. Delpy, and E. O.R. Reynolds, "Quantification of adult cerebral hemodynamics by near-infrared spectroscopy," *J. Appl. Physiol.* **77**, 2753-2760 (1994).
12. B. Chance, "Near-infrared images using continuous, phase-modulated, and pulsed light with quantitation of blood and blood oxygenation," *Ann. N. Y. Acad. Sci.* **839**, 29-45 (1998).
13. J. Fishkin, P. T. C. So, A. E. Cerussi, S. Fantini, M. A. Franceschini-Fantini, and E. Gratton, "Frequency-domain method for measuring spectral properties in multiple-scattering media: methemoglobin absorption spectrum in a tissuelike phantom," *Appl. Opt.* **34**, 1143-1155 (1995).
14. R. A. Weersink, J. E. Hayward, K. R. Diamond, and M. S. Patterson, "Accuracy of noninvasive *in vivo* measurements of photosensitizer uptake based on a diffusion model of reflectance spectroscopy," *Photochem. Photobiol.* **66**, 326-335 (1997).
15. B. Beauvoit, S. M. Evans, T. W. Jenkins, E. E. Miller, and B. Chance, "Correlation between the Light Scattering and the Mitochondrial Content of Normal Tissues and Transplantable Rodent Tumors," *Anal. Biochem.* **226**, 167-174, (1995).
16. A. M. K. Nilsson, C. Sturesson, D. L. Liu, and S. Andersson-Engels, "Changes in spectral shape of tissue optical properties in conjunction with laser-induced thermotherapy," *Appl. Opt.*, **37**, 1256-1267 (1998).
17. G. Zonios, L. T. Perelman, V. Backman, R. Manoharan, M. Fitzmaurice, J. Van Dam, and M. S. Feld, "Diffuse reflectance spectroscopy of human adenomatous colon polyps *in vivo*," *Appl. Opt.*, **38**, 6628-6637 (1999).
18. J. R. Mourant, J. P. Freyer, A. H. Hielscher, A. A. Eick, D. Shen, and T. M. Johnson, "Mechanisms of light scattering from biological cells relevant to noninvasive optical-tissue diagnostics," *Appl. Opt.*, **37**, 3586-3593 (1998).
19. H. Jiang, J. Pierce, J. Kao, and E. Sevick-Muraca, "Measurement of particle-size distribution and volume fraction in concentrated suspensions with photon migration techniques," *Appl. Opt.*, **36**, p3310-3318 (1997).
20. H. Jiang, G. Marquez and L. V. Wang, "Particle sizing in concentrated suspensions by use of steady-state, continuous-wave photon-migration techniques," *Opt. Lett.*, **23** (5), 394 -396 (1998).
21. N. Sato, K. Takenobu, S. Motoaki, K. Sunao, A. Hiroshi, and B. Hagihara, "Measurement hemoperfusion and oxygen sufficiency in gastric mucosa *in vivo*," *Gastroenterology* **76**, 814-819 (1979).
22. W. T. Knoefel, N. Kollias, D. W. Rattner, N. S. Nishioka, and A. L. Warshaw, "Reflectance spectroscopy of pancreatic microcirculation," *J. Appl. Physiol.* **80**, 116-123 (1996).
23. M. Ikeda and A. Matsushita, "Reflectance of rat brain structures mapped by an optical fiber technique," *J. Neurosci. Methods* **2**, 9-17 (1980).
24. R. Marchesini, M. Brambilla, C. Clemente, M. Maniezzo, A. E. Sichirollo, A. Testori, D. R. Venturoli, and N. Cascinelli, "In vivo spectrophotometric evaluation of neoplastic and non-neoplastic skin pigmented lesions. I. Reflectance measurements," *Photochem. Photobiol.* **53**, 77-84 (1991).
25. J.R. Mourant, I.J. Bigio, J. Boyer, T.M. Johnson, and T. Shimada, "Spectroscopic diagnosis of bladder cancer with elastic light scattering," *Lasers Surg. Med.* **17**, 350-357 (1995).
26. J.R. Mourant, I.J. Bigio, J. Boyer, T.M. Johnson, and J. Lacey, "Elastic scattering spectroscopy as a diagnostic for differentiating pathologies in the gastrointestinal tract: preliminary testing," *J. Biomed. Opt.* **1**, 192-199 (1996).
27. Z. Ge, K. T. Schomacker, and N. S. Nishioka, "Identification of colonic dysplasia and neoplasia by diffuse reflectance spectroscopy and pattern recognition techniques," *Appl. Spectrosc.* **52**, 833-839 (1988).
28. C. A. Giller, M. Johns, H. Liu, "Use of an intracranial near-infrared probe for localization during stereotactic surgery for movement disorders," *J. Neurosurg.* **93**, 498-505 (2000).
29. C. A. Giller, H. Liu, P. Gurnani, S. Victor, U. Yazdani, and D. C. German, "Validation of a near-infrared probe for detection of thin intracranial white matter structures," *J. Neurosurg.* **98**, 1299-1306 (2003).
30. J. R. Mourant, T. M. Johnson, G. Los, and I. J. Bigio, "Non-invasive measurement of chemotherapy drug concentrations in tissue: preliminary demonstrations of *in vivo* measurement," *Phys. Med. Biol.* **44**, 1397-1417 (1999).
31. L. H. Wang, S. L. Jacques, and L. Q. Zheng, "MCML-Monte Carlo modeling of photon transport in multi-layered tissues," *Comput. Methods Programs Biomed.* **47**, 131-146 (1995).
32. L. H. Wang, S. L. Jacques, and L. Q. Zheng, "CONV-Convolution for responses to a finite diameter photon beam incident on multi-layered tissues," *Comput. Methods Programs Biomed.* **54**, 142-150 (1997).
33. F.P. Bolin, L.E. Preuss, R.C. Taylor, and R.J. Ference, "Refractive index of some mammalian tissue using fiber optic cladding method," *Appl. Opt.* **28**, 2297-2303 (1989).
34. F. Bevilacqua, D. Piguet, P. marguet, J.D. Gross, B.J. Tromberg, and C. Depeursinge, "In vivo local determination of tissue optical properties: applications to human brain," *Appl. Opt.* **38**, 4939-4950 (1999).
35. Maureen Johns and Hanli Liu, "Calculating the reduced scattering coefficient of turbid media from a single optical reflectance signal," *SPIE Proc.* **4958**, to appear, 2003.

36. A. H. Hielscher, H. Liu, B. Chance, F. K. Tittel, and S. L. Jacques, "Time Resolved Photon Emission from Layered Turbid Media," *Appl. Opt.* **35**, 719-728 (1996).
  37. B.C. Wilson and S.L. Jacques "Optical reflectance and transmittance of tissue: Principle and Applications," *Journal of quantum electronics.* **26**, 2186-2199 (1990).
  38. Prem Gurnani, "Near Infrared Spectroscopic Measurement of Human and Animal Brain Structures," M.S. Thesis, The University of Texas at Arlington, Arlington, TX, May 2003.
- 

## 1. Introduction

Steady-state diffuse reflectance spectroscopy is a simple spectroscopic technique that has been used to study optical properties of biological tissue [1,2], to identify tissue types [3,4,5], to diagnose cancer [6], and to monitor drug delivery processes [7]. Basically, light that is delivered to the tissue surface undergoes multiple elastic scattering and absorption; part of it returns to the surface as diffuse reflectance, carrying quantitative information on the structure and composition of the measured tissue [8,9]. Wavelength-dependent absorption can be used to quantify the concentrations of biologically important chromophores, such as hemoglobin, myoglobin, water, fat, and near-infrared-absorbing drugs [10-14]. Light scattering, on the other hand, can provide information [15] in real time on scatterer sizes [16-18] and densities [19,20] within the measured tissue, providing a possible marker used in optical biopsy and optical identifications of tissue.

To benefit fully from spectroscopic measurements, a methodology is needed to associate the spectral features with the underlying biochemistry and morphology. A variety of reports of measurements on a variety of human and animal tissues, both *in vivo* and *in vitro*, have been published: semi-empirical models have been used to determine blood content and hemoglobin (Hb) oxygen saturation in rat gastric mucosa [21] and rat pancreas [22], differences in the diffuse reflectance of rat brain were characterized empirically [23], and empirical analysis was also employed to study human tissues *in vivo*, such as skin [24], bladder [25], and colon [26,27]. The results confirm that optical reflectance of tissue provides valuable physiological/pathological information, but the scattering nature of light limits the accuracy of the spatial information obtained.

For the last few years, we have utilized diffuse reflectance spectroscopy (also called light scattering spectroscopy) as a tissue classification means to differentiate gray and white matter in the human brain to assist functional neurosurgery [3,28,29]. A near infrared (NIR) fiber optic probe used in the present study contains one 100- $\mu\text{m}$  (or 400- $\mu\text{m}$ ) source fiber and one 100- $\mu\text{m}$  (or 400- $\mu\text{m}$ ) detection fiber with a separation of  $\sim 100\ \mu\text{m}$  (or  $\sim 400\ \mu\text{m}$ ). This kind of optical probes enables us to obtain one-dimensional (1-D) spatial mapping profiles along the neuro-surgical tracks to provide anatomical information in real time, based on the fact that gray matter, white matter, and cerebral spinal fluid (CSF) within the brain scatter light quite distinctly. Our previous studies have shown good consistency between the optically obtained spatial profiles and the actual anatomical profiles based on the post-operative MRI images [28]. A recent report by Giller et al has demonstrated that such an NIR probe can reliably detect submillimeter layers of intracranial white matter structures [29], based on rodent models, phantom models, and computer simulations.

Because of the scattering nature of light within tissue, the measured reflectance results from the volume that is interrogated by the light in front of the probe tip, causing an averaged or convoluted effect in measured data and worsening the spatial resolution. Knowledge on the detection depth interrogated by the optical field with such a small source-detection separation is limited [30], and a concept of "lookthrough distance" and its initial exploration have been introduced and discussed [29]. This paper, indeed, presents a more quantitative and thorough study for the laboratory phantom development and computer simulations to address the "lookthrough distance" or "look ahead distance" of an NIR small-separation probe.

In principle, an optically interrogated volume lies straight ahead at an optical probe tip when two (or more) fibers within the probe are placed within tissue, as shown in Fig. 1. The maximal length of the interrogated volume ahead of the probe highly depends on the optical properties of the measured sample and the separation of the source and detection fibers. For convenience, we define a term of “Look Ahead Distance” (LAD) to represent the distance between the tip of the probe and the maximal forward depth, within which the probe can still detect the reflectance signal (Fig. 1) when the probe is within the tissue. The LAD defined here is identical to “the lookthrough distance” given in Ref. 29.

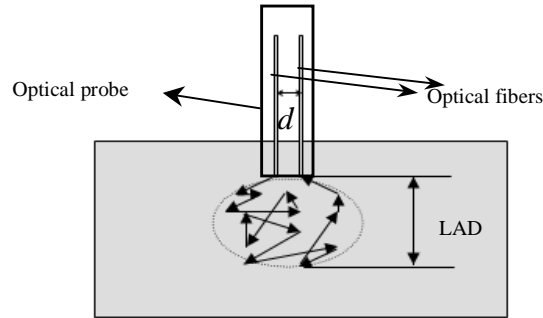


Fig.1. Demonstration of the Look Ahead Distance (LAD) for a small separation probe. The dashed profile curve outlines the tissue volume that is interrogated by the light pattern, and  $d$  is the separation of the source and detector fibers.

The purpose of this study was to develop an experimental methodology to obtain a quantitative expression for the LAD of our currently used probes in order to quantify the probes’ resolution. The approach used in this study was based on both laboratory phantom measurements and Monte Carlo simulations, leading to empirically derived equations for the LAD as a function of reduced scattering coefficient ( $\mu_s'$ ) of the measured tissue for a 400- $\mu\text{m}$  fiber probe (i.e., a probe containing two of 400- $\mu\text{m}$  fibers with a separation of  $\sim 400 \mu\text{m}$  between the fibers) and 100- $\mu\text{m}$  probe. The methodology and experimental protocols developed here can be applied in obtaining the LADs of other optical probes, which are needed to improve the spatial resolution of the optical probes for better surgery guidance. Furthermore, the knowledge and quantification learned on LAD of a tissue-sensing probe would provide us with better understanding of light interaction with tissue within a millimeter distance.

## 2. Monte Carlo simulations

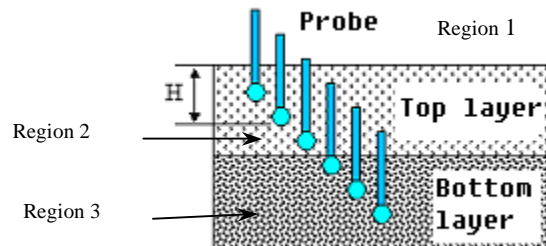


Fig. 2. Monte Carlo simulation model: the top and bottom layer have a thickness of 10 mm and 13 mm, respectively. Region 1 represents the top entry medium, Region 2 is for the top layer, and Region 3 is for the bottom layer.

To predict the optical reflectance from the human brain and the LAD crossing a boundary within tissue, we employed the Monte Carlo simulation code that was provided by Wang and Jacques through the internet [31,32]. Two-layer models were used in the simulation to represent white matter and gray matter with various input parameters of reduced scattering coefficient,  $\mu_s'$ , and absorption coefficient,  $\mu_a$ . As shown in Fig. 2, the thickness of the top layer was 10 mm, the bottom layer was 13 mm, Regions 1, 2, and 3 represent the top entry medium, the top layer of the model, and the bottom layer, respectively.

In the simulations, the input number of photons was 1,000,000, and the indexes of refraction ( $n$ ) for both top and bottom layers were chosen to be  $\sim 1.38$  [33] since both of them were simulating brain tissues. The mean cosine of the scattering angle ( $g$ ) for tissue was 0.9. The simulated separation between the source and detector was 400  $\mu\text{m}$ , and the output data were normalized at a certain depth of the 2-layer model. Since the NIR probe is always placed within the tissue volume for both the phantom and the animal/human studies, the simulation input parameters were chosen in such a way that there existed no mismatch of  $n$  at the entry boundary, namely, the boundary between Region 1 and Region 2 as shown in Fig. 2. Specifically, we used 1.38 for the top entry medium so that there is no air-tissue interface (or mismatch of  $n$ ) when the injected photons enter the top layer. Furthermore, the reflectance signal was recorded as the simulated probe was moving from the surface of the top layer into the bottom layer. The moving step size in depth was 1 mm when the probe was 0 to 7 mm away from the top surface, and 0.2 mm as the step size when the probe was crossing the boundary between the two layers, namely, 7 mm to 11.6 mm away from the top surface.

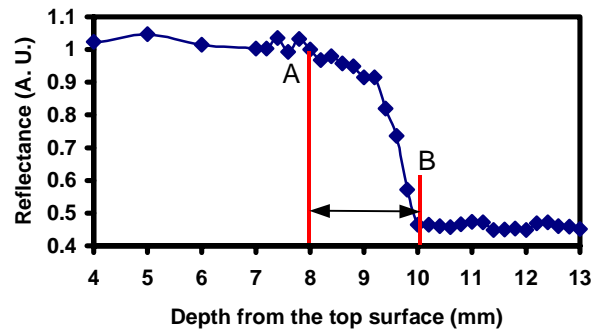


Fig. 3. Simulated reflectance versus depth for determination of the LAD using a 2-layer model. The top layer is 10 mm thick as white matter with  $\mu_s'=10 \text{ cm}^{-1}$  and  $\mu_a=0.1 \text{ cm}^{-1}$ , and the bottom layer is 13 mm as gray matter with  $\mu_s'=5 \text{ cm}^{-1}$  and  $\mu_a=0.2 \text{ cm}^{-1}$ . The data points were normalized to the reflectance at 7 mm with a source-detection fiber separation of 400 microns.

Figure 3 shows the corresponding simulated reflectance profile of a 2-layer model with white matter and gray matter being the top and bottom layer, respectively. The top layer has<sup>34</sup>  $\mu_s'=10 \text{ cm}^{-1}$  and  $\mu_a=0.1 \text{ cm}^{-1}$ , and the bottom layer has  $\mu_s'=5 \text{ cm}^{-1}$  and  $\mu_a=0.2 \text{ cm}^{-1}$ . The data points presented here are all normalized to the reflectance at 7 mm. As seen here, the reflectance profile starts to decrease slowly at around 8 mm and flattens out at 10 mm, indicating that the probe enters the bottom layer completely at the depth of 10 mm. We define the LAD to be the distance between points A and B, at which the normalized reflectance data start to deviate from or approach to a flattened region, with a deviation larger than 2 times of the standard deviation of the normalized reflectance data within the flat region. The LAD in this case is 1.9 mm.

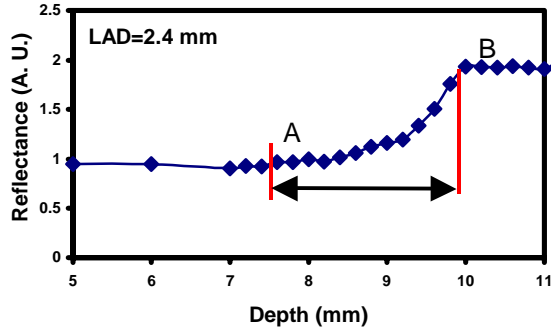


Fig. 4. Simulated reflectance output versus depth for determination of the LAD of another 2-layer model. The top layer is 10 mm as gray matter with  $\mu_s'=5 \text{ cm}^{-1}$  and  $\mu_a=0.2 \text{ cm}^{-1}$ , and the bottom layer measured is from 10 mm to 11 mm as white matter with  $\mu_s'=10 \text{ cm}^{-1}$  and  $\mu_a=0.1 \text{ cm}^{-1}$ . The data points from 5 mm to 13 mm depths were normalized to the reflectance at 7 mm. The separation is 400 microns between the source and detection fiber.

Figure 4 shows another case, similar to that in Fig. 3 except that the two layers here have been inverted: the 10-mm top layer simulates gray matter with  $\mu_s'=5 \text{ cm}^{-1}$  and  $\mu_a=0.2 \text{ cm}^{-1}$ , and the 13-mm bottom layer mimics white matter with  $\mu_s'=10 \text{ cm}^{-1}$  and  $\mu_a=0.1 \text{ cm}^{-1}$ . Following the same definition, the LAD for Fig. 4 is 2.4 mm. It is noticed that the LAD shown in Fig. 4 has been increased as the  $\mu_s'$  value of the top layer is decreased, implying that a less dense scattering medium will result in a longer LAD. In order to compare the LADs between the simulation results and the experiments, more Monte Carlo simulations have been performed using a variety of  $\mu_s'$  and  $\mu_a$  values, which were observed in the phantom experiments. The calculated LADs from the simulation data are listed in Table 1, and the given  $\mu_s'$  and  $\mu_a$  values in Table 1 were all for the top layers.

Table 1. The Look-ahead distance (LAD) determined from Monte Carlo simulations. The top layer was 10 mm thick, and the bottom layer was 13 mm with  $g=0.9$  and  $n=1.38$ .

$\mu_s' \text{ (cm}^{-1}\text{)}$	$\mu_a \text{ (cm}^{-1}\text{)}$	LAD (mm)
4.41	0.0318	2.80
8.70	0.0308	2.32
12.99	0.0298	1.98
21.56	0.0278	1.62
25.85	0.0268	1.48
30.14	0.0258	1.28
34.42	0.0248	1.26

Indeed, a recent Monte Carlo study has shown [35] that the absorption effect on the reflectance determined by an NIR probe with a 400- $\mu\text{m}$  separation can be reasonably neglected, when  $\mu_a$  values of the measured sample are equal to or less than  $0.5 \text{ cm}^{-1}$ . This is expected since in the NIR range,  $\mu_s'$  values of tissue are much larger than  $\mu_a$  values, resulting in a minimal effect caused by absorption, particularly with a small detection distance between the source and detector. In the following sections, therefore, we can ignore the dependence of reflectance,  $R$ , on absorption properties of the phantoms as long as their  $\mu_a$  values are less than  $0.5 \text{ cm}^{-1}$ .

### 3. Materials and methods for phantom studies

To study the LAD of the probe experimentally, we developed a two-layer soft tissue phantom that permits the probe to go through from the top layer to the bottom layer. The basic materials consisted of Gelatin powder and Intralipid, and the respective concentrations resulted in different hardness and scattering properties of the phantom [36]. Basically, we utilized two types of the phantoms: solid-solid (or gelatin-gelatin) and liquid-solid (or Intralipid-gelatin) phantoms. The  $\mu_s'$  and  $\mu_a$  values of each layer of the phantoms were measured by an ISS oximeter (96208, ISS, Champaign, IL).

#### 3.1 Multi-layer tissue phantom preparation

**Bottom Gelatin Layer:** 15 grams of Gelatin powder (Sigma, St Louis, MO, USA) made from porcine skin were added into 200 ml of boiling water and was dissolved completely by stirring. After the solution was cool down, the Intralipid (IL) solution with a certain concentration was added to the prepared gelatin solution and was allowed for the formation of gel. The percentage concentration of the IL used was varied depending on the required  $\mu_s'$ . The  $\mu_s'$  of the mimicked gray matter is kept low in comparison to the other layer.

**Top Gelatin Layer:** to generate gelatin-gelatin phantoms, a process similar to that in making the bottom layer was repeated for the top layer, except that the concentration of Intralipid used was lower or higher than that of the bottom layer in order to create the scattering contrast between the two layers. After the bottom layer was completely gelatinized, the prepared gelatin-Intralipid solution for the top layer was added on top of the bottom layer, leading to a gelatin-gelatin model after the solidation process was complete.

**Top Liquid Layer:** by having different concentrations of Intralipid solutions placed on top of the bottom phantom, we could generate a 2-layer, liquid-gelatin model. In this way, it was easier and quicker to vary the optical properties of the top layer. Although a mismatch of refractive index between the liquid and gelatin may exist, the experimental data (given in later sections) have shown minimal effects due to this mismatch.

The lifetime of such gelatin phantoms was relatively short, ~ one week; the phantoms were refrigerated during the week to prevent them from being decayed fast. After a week, they tend to lose water, becoming hard and changing their optical properties.

#### 3.2 ISS oximeter

The ISS oximeter works on the principle of diffusion theory, which models photon transport in tissue. Diffusion theory is appropriate for a medium dominated by light scattering rather than absorption, so each photon undergoes many scattering events before being terminated by an absorption event. In this case, each photon has a relatively long lifetime, allowing the photon to engage in a random walk within the medium. The ISS oximeter is basically a frequency-domain, multiple-distance (FDMD) based instrument, capable of measuring the absolute absorption and reduced scattering coefficients for our gelatin-gelatin phantoms.

#### 3.3 Experimental setup for phantom measurements

The experimental setup for laboratory phantom measurements is shown in Fig. 5. The light delivering fiber was connected to a tungsten-halogen light source with a spectral range of 360 nm - 2  $\mu$ m, (LS-1, Ocean Optics, Inc., Dunedin, FL), and the detecting fiber was connected to a linear CCD spectrometer (USB2000, Ocean Optics, Inc., Dunedin, FL) with a wavelength range from 350-850 nm. The instrument system also included a data acquisition card (DAQ-1200), a linear actuator (TA-35H-100-L-R-S, Torrance, CA), a stepper motor driving for the actuator (National Instruments: MID 7604/7602, 4/2 axis), and a laptop computer. The optical probe with one source and one detection fiber (see the cross section in Fig. 5) was fixed on the stage of the actuator. The outer diameter of the stainless steel probe tube was 1.3

mm, and the length was ~25 cm. The spectrometer collected the optical signals as the optical probe moved into the phantom with a given step size.

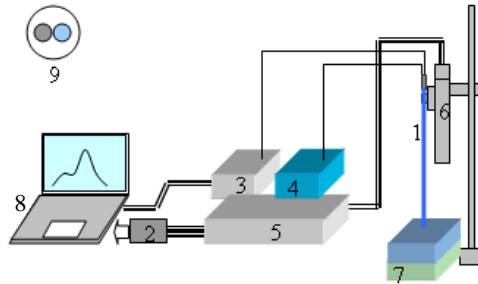


Fig. 5. The experimental setup consists of (1) an optical probe containing two 400- $\mu\text{m}$  fibers, (2) a data acquisition card, (3) a USB CCD spectrometer, (4) a broadband light source, (5) a power supply and control for the actuator, (6) an automatic linear actuator, (7) a laboratory tissue phantom, (8) a laptop computer, and (9) a cross section of the fiber probe.

Following our previous approach [3,28], the slope of the spectral data between 700 nm and 850 nm in the NIR range was used here as a relative index to represent the reflectance intensities measured from the various phantoms. The slope in the chosen range is directly proportional to the reflectance intensities with numerous data points, which offer better statistics for the measurement. In calibration, the reflectance signals,  $R$ , were calculated by  $R = (\text{signal-dark}) / (\text{reference-dark})$ , where “dark” was the signal due to the instrument system only and about 1~5% of the sample signal. The dark data used in the data process were taken from the corresponding readings when the light source was off. The reference was taken from a standard white sample (Labsphere, North Sutton, NH), which has nearly 99.9% reflection with a flat spectrum, for all *in vitro* and *in vivo* measurements. It is important to note that to be accurate, the signal, dark, and reference used for  $R$  calculation needed to be collected with the same integration time of the CCD spectrometer.

#### 4. Experimental results of the phantom study

##### 4.1 Intralipid-gelatin phantom model

Intralipid-gelatin phantoms were developed to study the dependence of the LAD on the optical properties of the top layer. The concentrations of top Intralipid solutions were varied while the bottom gelatin had fixed values of the scattering and absorption coefficient. Figures 6(a) and 6(b) show two examples of normalized slope output versus depth for quantification of the LAD of the intralipid-gelatin model. The LADs were determined from the normalized slope profiles in the same way as those used in the Monte Carlo simulations, as shown in Figs. 3 and 4.

Four sets of bottom gelatin phantoms with the  $\mu_s'$  values ranging from 1.7  $\text{cm}^{-1}$  to 11.8  $\text{cm}^{-1}$  were prepared (Table 2). For each of the gelatin sets, seven solutions with Intralipid concentrations of 0.5% to 4% were used to create the  $\mu_s'$  values of 4.41  $\text{cm}^{-1}$  to 34.42  $\text{cm}^{-1}$  for the top layers to quantify the respective LADs. Moreover, the  $\mu_a$  and  $\mu_s'$  values of the bottom and top layers were measured with the ISS oximeter at wavelength 750 nm, as listed in Table 2, and at 830 nm. Besides the  $\mu_a$  and  $\mu_s'$  values of the top and bottom layers, Table 2 shows the mean values of the observed LADs with the standard deviation for the 400- $\mu\text{m}$  fiber probe from the experiments. The mean LADs were obtained from 4 runs made in different tracks of the model for each concentration with the integration time being 10 ms. Table 2 clearly

demonstrates that the LADs depend strongly on the scattering properties of the top layer, but little on those of the bottom layer.

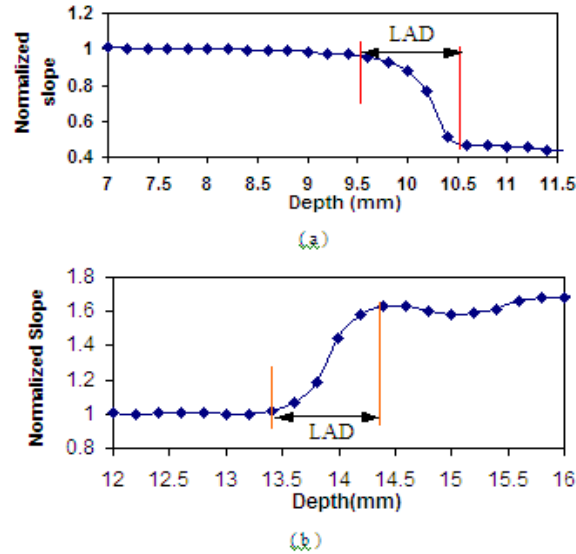


Fig. 6. Experimental results of normalized slope output versus depth for determination of the LAD of a 2-layer model. (a): the top layer is a simulated white matter, and bottom layer is a simulated gray matter. (b): the top layer is a simulated gray matter and bottom is a white matter. The data points were normalized at 7 mm. The source-detector fiber separation is 400 microns.

Table 2. Values of the observed LADs (400-micron fiber probe). TL: top layer; BL: bottom layer; IL: Intralipid. Number of measurements = 4 for each group

% IL Concentration (TL)	$\mu_s'$ ( $\text{cm}^{-1}$ )	$\mu_a$ ( $\text{cm}^{-1}$ )	LAD (mm)			
			2.5% IL (BL) $\mu_s' = 11.8 \text{ cm}^{-1}$	2% IL (BL) $\mu_s' = 7.4 \text{ cm}^{-1}$	1.5% IL (BL) $\mu_s' = 5.1 \text{ cm}^{-1}$	0.5% IL (BL) $\mu_s' = 1.7 \text{ cm}^{-1}$
0.5	4.41	0.0318	$2.8 \pm 0.2$	$3.0 \pm 0.1$	$2.8 \pm 0.2$	$2.8 \pm 0.3$
1	8.7	0.0308	$2.3 \pm 0.2$	$2.7 \pm 0.2$	$2.2 \pm 0.1$	$2.3 \pm 0.2$
1.5	12.99	0.0298	$2.0 \pm 0.2$	$2.2 \pm 0.2$	$2.0 \pm 0.3$	$2.1 \pm 0.3$
2.5	21.56	0.0288	$1.5 \pm 0.1$	$1.4 \pm 0.2$	$1.7 \pm 0.3$	$1.8 \pm 0.1$
3	25.85	0.0278	$1.7 \pm 0.2$	$1.5 \pm 0.2$	$1.6 \pm 0.2$	$1.7 \pm 0.3$
3.5	30.14	0.0268	$1.3 \pm 0.3$	$1.4 \pm 0.2$	$1.5 \pm 0.2$	$1.6 \pm 0.2$
4	34.42	0.0258	$1.4 \pm 0.2$	$1.4 \pm 0.2$	$1.5 \pm 0.2$	$1.7 \pm 0.1$

As another way to further understand Table 2, Fig. 7 shows the dependence of LADs on the  $\mu_s'$  values of the top layers for each of the four bottom gellatins. The average LADs over the four sets of the data (plotted by the solid line) can be fitted by a logarithmic equation ( $R^2 = 0.983$ ) and expressed in mm as:

$$LAD_{750\text{-nm}} = -0.70 \ln(\mu_s') + 2.26 \quad (1)$$

where  $\mu_s'$  is the reduced scattering coefficient of the measured samples at 750 nm in  $\text{mm}^{-1}$ , and  $LAD_{\text{NIR}}$  represents the LAD determined experimentally in mm. Equation (1) indicates that the LAD of a fiber probe with the NIR light will decrease as the  $\mu_s'$  value of measured sample increases. Furthermore, since light scattering in the NIR range (i.e., 700-850 nm) is weakly

wavelength-dependent,  $LAD_{750\text{-nm}}$  here can be approximated to represent an average value of LAD over this wavelength range, namely  $LAD_{750\text{-nm}} = LAD_{\text{NIR}}$  in mm.

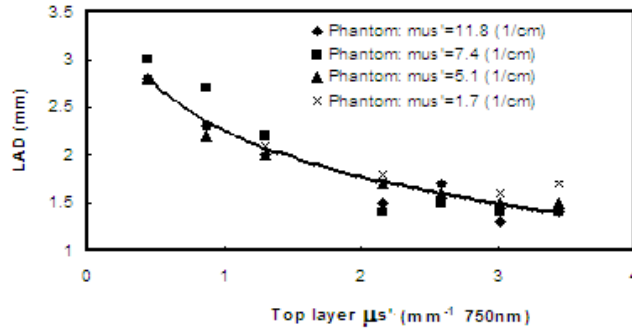


Fig. 7. The relationship of the LAD and the scattering property of top layer,  $\mu_s'$ . Four series of the data points shown were the average LADs obtained from the four solid bottom layers with different Intralipid concentrations as the top layers. The fitting curve gives the quantitative LAD equation, eq. (1), for the Intralipid-Gelatin phantom model.

#### 4.2 Gelatin-gelatin phantom model

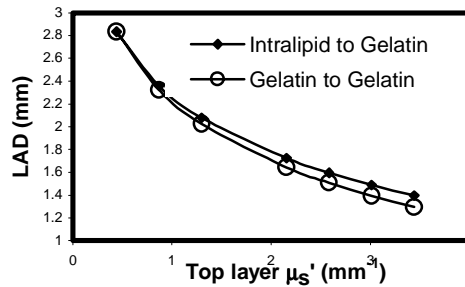


Fig. 8 Experimentally determined LADs using gelatin-gelatin and intralipid-gelatin models.

In order to simulate more realistic brain tissues, soft gelatin-gelatin phantoms were made and measured with the values of  $\mu_s'$  ranged from  $2 \text{ cm}^{-1}$  to  $10 \text{ cm}^{-1}$ . These values were reported from children patients in vivo [34]. Although these values seem to be smaller than those reported for the adult brain, the derived expression can be extended for a large range of  $\mu_s'$  for adults. Following the calculation and calibration procedures same as those used for intralipid-gelatin samples, we measured the gelatin-gelatin samples and arrived at Eq. (2):

$$LAD_{\text{NIR}} = -0.75 \ln(\mu_s') + 2.22 \quad (2)$$

Figure 8 shows the comparison between the two phantom models, demonstrating that the gelatin-gelatin and intralipid-gelatin models are reasonably consistent.

#### 4.3 Comparison between the simulation and experiment results

Figure 9 demonstrates the consistent values of the LADs obtained from the Monte Carlo simulations and from Eq. (2) for a  $400\text{-}\mu\text{m}$  fiber probe, with  $\mu_s' = 10 \text{ cm}^{-1}$  and  $\mu_a = 0.1 \text{ cm}^{-1}$  for the simulated white matter, and  $\mu_s' = 5 \text{ cm}^{-1}$  and  $\mu_a = 0.2 \text{ cm}^{-1}$  for the simulated gray matter. This figure also illustrates that the LAD is larger when the probe is in the simulated gray layer and smaller when the probe is in the simulated white layer. A relative error of 10% for LAD

is considered because of the uncertainty in selecting the starting and ending points to determine the LAD from the reflectance profiles.

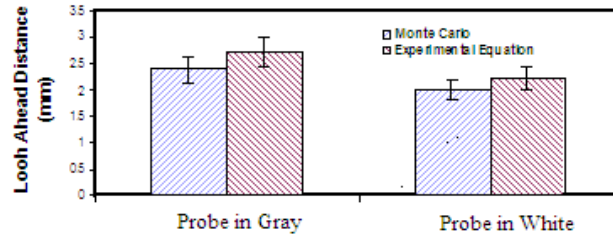


Fig. 9. Comparison of the LADs obtained from both the simulation and the fitting equation.

## 5. Discussion

### 5.1 Comparison of the penetration depth with the LAD

If the source and detector separation,  $d$ , of an optical probe is larger than a few times of transport mean free path (mfp), diffusion theory can be valid to quantify the penetration depth

( $d_p$ ) of the optical signal, expressed as [37]  $d_p = \frac{1}{\sqrt{3\mu_a(\mu_s' + \mu_a)}}$  with  $mfp=1/(\mu_s'+\mu_a)$ .

When  $d$  of a fiber probe is on the same order as mfp, however, diffusion theory does not hold to correctly interpret light propagation in tissue near the probe tip. This is the case when the small-separation NIR probe is used, where  $d$  is between 100-400  $\mu m$  and is near or shorter than an average mfp of tissue ( $\sim 0.5-1$  mm). The meaning of LAD is different from that of  $d_p$  in that LAD is the maximal vertical distance from the probe tip, within which the reflectance probe can detect the underlying tissue based on light scattering, whereas  $d_p$  is the distance from the source tip, at which the light intensity is decreased to 37% of its original value. In order to quantify the LAD of an optic fiber probe, we had to take an experimental and computer simulation approach to empirically arrive at a relationship between the LAD and  $\mu_s'$  of the measured sample in the NIR range. Further theoretical study is needed if one wishes to prove the expression mathematically.

### 5.2 Validity and Usefulness of the Expressions for LAD

This study was initiated, particularly focusing on biomedical applications of a small-separation, fiber optic probe to detect/identify tissue types using NIR light. Equations (1) and (2) for the LAD quantification were obtained empirically only for one of our NIR probes, depending on the fiber size, fiber separation, and probe configuration. In general, the LAD also depends on wavelength and is relatively constant in the NIR range, as mentioned earlier. In the wavelength range of 500-650 nm, however, the LAD of a fiber probe will vary largely with wavelength because of high variation in light absorption due to the existence of hemoglobin in tissue. Similar Monte Carlo simulations in the wavelength range of 500-650 nm can be conducted to test whether Eqs. (1) and (2) still hold.

Although the expression of LAD developed here is specifically only for one of the probes, the methodology and experimental protocols are general and can be applied to other probes for their LAD quantifications. Indeed, we have also obtained a LAD expression for a thinner probe containing two of 100- $\mu m$  fibers with a center-to-center separation of  $\sim 100$   $\mu m$ , as given below:

$$LAD_{NIR}(100\text{-}\mu m) = -0.44 \ln(\mu_s') + 1.30, \quad (3)$$

where  $\mu_s'$  are in  $\text{mm}^{-1}$ , and LAD is in mm. Comparison between Eqs. (2) and (3) demonstrates that a thinner probe with a shorter separation has a shorter LAD, as one normally expects. Overall, we learned from this study that either the Monte Carlo simulation or experimental phantom measurement is adequate to obtain the quantitative LAD expression.

Although Eqs. (2) and (3) are sample-dependent, but they should be valid relatively broadly for biological tissues as long as NIR light is used for the sensing probe. Based on our simulation and experimental data, the following estimated conditions provide an approximate range of validity for the empirical expressions:  $g > 0.9$ , reduced scattering albedo ( $= \frac{\mu_s'}{\mu_s' + \mu_a}$ )  $> 0.89$ ,  $\mu_s' > 4 \text{ cm}^{-1}$  and  $\mu_a < 0.5 \text{ cm}^{-1}$ . In general, almost all of the respective parameters of biological tissues fall within the given ranges when NIR light is utilized.

### 5.3 Interpretation of *in vivo* Measurements

Now, with the understanding that the LAD depends highly on  $\mu_s'$  of the measured area, to be large if  $\mu_s'$  is small and small if  $\mu_s'$  is large, we expect that the LAD is relatively larger in gray matter than that in white matter. This is exactly what we observed in the animal validation experiments [29], where we have observed a slow rising and fast falling trend of the slope profile when the probe passes through a combined 3-layer brain tissue section of gray-white-gray matter. The slow rising feature is attributed to a larger LAD in gray matter when the probe approaches to the gray-white matter junction, whereas the fast falling feature is due to a shorter LAD in white matter when the probe leaves from the white matter to enter another underlying layer of gray matter. Given the fact that the difference between LADs for high and low  $\mu_s'$  is real but small, it is not significant for clinical application, particularly for neurosurgery guidance [29]. Our recent study has shown that the  $\mu_s'$  values of gray and white matter of the human brain are relatively large [38], giving rise to a relatively small LAD and thus resulting in a spatial resolution better than 1 mm.

The quantitative LAD expression will allow us to interpret the *in vivo* data better and further to improve the spatial resolution of the 1-D neurostructural mapping, in the future, by de-convolving the measured data with the LAD profile. In order to conduct an actual de-convolution process, a possible profile function to represent the probe's 'blur function' will be chosen according to the LAD, which serves as the point-spread function (PSF). Then, the actual measured NIR profiles can be de-convolved with the probe's PSF to provide 1-D mapping for biological applications with a better spatial resolution. An exploratory example is given in Ref. [29] to demonstrate the principle and importance of deconvolution process for neurosurgery guidance.

## 6. Conclusion

Quantification of the LAD of a fiber optic probe is important to quantify the spatial resolution to guide neurosurgery. In this work, two kinds of 2-layer tissue models have been developed so as to determine the LAD, and Monte Carlo simulations were also used to confirm the experimental findings. The study shows that a relatively simple expression can be arrived to associate the LAD with the scattering property of the measured tissue for the 400- $\mu\text{m}$  (and 100- $\mu\text{m}$ ) probe, and that the expression is consistent between the experiment and simulation results. Particularly, absorption has little significant effect on the LAD when using NIR light, and the LAD value of biological tissues for the 400- $\mu\text{m}$  probe ranges from 1 to 2 mm or even larger, depending on the actual measurement location.

## Acknowledgments

The authors acknowledge the support of a National Institute of Neurological Disorders and Stroke Grant No. NS40874-02.